

# Chronic optical access through a polished and reinforced thinned skull

Patrick J Drew<sup>1-3</sup>, Andy Y Shih<sup>1</sup>, Jonathan D Driscoll<sup>1</sup>, Per Magne Knutsen<sup>1</sup>, Pablo Blinder<sup>1</sup>, Dimitrios Davalos<sup>4</sup>, Katerina Akassoglou<sup>4,5</sup>, Philbert S Tsai<sup>1</sup> & David Kleinfeld<sup>1,6,7</sup>

**We present a method to form an optical window in the mouse skull that spans millimeters and is stable for months without causing brain inflammation. This enabled us to repeatedly image blood flow in cortical capillaries of awake mice and determine long-range correlations in speed. We also repeatedly imaged dendritic spines, microglia and angioarchitecture, as well as used illumination to drive motor output via optogenetics and induce microstrokes via photosensitizers.**

Chronic observation and manipulation of cells in the cortex is integral to studies on neurons, glia and microvasculature. An increasingly popular application involves the use of *in vivo* two-photon laser scanning microscopy (TPLSM) to image deep within the mammalian cortex through a window in the skull<sup>1</sup>. This window may be formed by a craniotomy<sup>2</sup>, in which a section of skull is removed and replaced with glass, or by thinning a section of the skull with a microsurgical blade<sup>3</sup>. Both methods have been used for chronic observation of fluorescently labeled neuronal processes<sup>3,4</sup> and microvasculature<sup>5</sup> yet have limitations. It has been suggested that cranial windows activate microglia and astrocytes as part of an inflammatory response<sup>6</sup> that can alter neuronal physiology<sup>7</sup> and pial blood vessels<sup>8</sup>, although these complications may relate to surgical finesse<sup>9</sup>. The thinned-skull procedure avoids the activation of microglia and astrocytes<sup>6</sup> yet access is limited to a very small area:  $\sim 0.2 \text{ mm}^2$  compared to  $1\text{--}10 \text{ mm}^2$  for a craniotomy. Further, sequential imaging sessions require skull rethinning to counteract bone regrowth, which limits the number of times that imaging can be performed and leaves the area under the thinned portion of skull mechanically vulnerable<sup>3</sup>. Thus there is a need for a technique that provides readily available optical access across a large area of the brain without the potential to induce inflammation.

We introduce a polished and reinforced thinned skull (PoRTS) procedure to create a large, chronically stable window in the skull. We attempted to satisfy four goals with this method: (i) optical clarity, sufficient for imaging with TPLSM as well as optogenetic control, without the need to intervene after the initial surgery; (ii) optical access across many square millimeters; (iii) mechanical stability for imaging in awake animals; and (iv) the absence of an inflammatory response.

Our basic idea was to mechanically thin the skull<sup>3</sup>, polish the cut surface to improve flatness and then fuse transparent cement and glass to the thinned bone to form a clear, rigid window. We designed the glass window to stabilize the thinned and thus weakened bone, and reasoned that both the mechanical stability and the fusion of the window to the bone would inhibit bone regrowth, thus preserving clarity. In detail, we thinned the skull with a high-speed burr to a final thickness of  $10\text{--}15 \mu\text{m}$ , polished it without direct pressure on the skull with a slurry of grit in artificial cerebral spinal fluid (ACSF) and then fused it to a cover glass with a thin layer of cyanoacrylate cement (Fig. 1a).

The optical transfer function for two-photon-excited fluorescence measured through the PoRTS window was modestly degraded compared to that measured using only a cover glass (Fig. 1b). The resolution varied across the window, presumably as a result of natural inhomogeneities in bone, with a radial width of  $0.7\text{--}1.0 \mu\text{m}$  (full width of half of the integrated intensity) and an axial resolution of  $\sim 3 \mu\text{m}$ . The TPLSM signal was diminished by a factor of  $e^{-1.5}$  by the thinned bone (Supplementary Fig. 1); this is equivalent to the loss in signal by imaging through  $150 \mu\text{m}$  of brain tissue<sup>10</sup>. Despite such caveats, we could repeatedly observe the dendritic spines of neurons expressing YFP both 2 d and several weeks after surgery (we analyzed two mice; Fig. 1c). Second, we repeatedly imaged subsurface brain microvessels in mice in which the plasma had been stained with fluorescein-conjugated dextran. We obtained good visibility up to  $250 \mu\text{m}$  below the pial surface for up to 3 months (35 mice; Fig. 1d). In a more stringent examination, we found that the pattern of subsurface microvascular architecture was stable when we imaged the same group of microvessels over 40 d through a PoRTS window (three fields across two mice; Fig. 1e). Consistent with the long-term optical clarity of subsurface brain structures, the PoRTS window impeded regrowth of the thinned skull as assayed by measuring skull thickness over time (Supplementary Fig. 2).

A critical biological assessment of the PoRTS window concerns the potential activation of microglia; these cells change their morphology in response to insults to the brain<sup>11</sup>. We used transgenic

<sup>1</sup>Department of Physics, University of California at San Diego, San Diego, California, USA. <sup>2</sup>Center for Neural Engineering, Department of Engineering Science and Mechanics, The Pennsylvania State University, University Park, Pennsylvania, USA. <sup>3</sup>Department of Neurosurgery, The Pennsylvania State University, University Park, Pennsylvania, USA. <sup>4</sup>Gladstone Institute of Neurological Disease, University of California, San Francisco, San Francisco, California, USA. <sup>5</sup>Department of Neurology, University of California, San Francisco, San Francisco, California, USA. <sup>6</sup>Graduate Program in Neurosciences, University of California at San Diego, San Diego, California, USA. <sup>7</sup>Center for Neural Circuits and Behavior, University of California at San Diego, San Diego, California, USA. Correspondence should be addressed to D.K. (dk@physics.ucsd.edu).

mice expressing enhanced GFP (EGFP) in microglia, that is, line *Cx3cr1<sup>EGFP/+</sup>*. At 2 d after surgery, which corresponds to the time when microglia are maximally active under a craniotomy<sup>6</sup>, we observed a diffuse, highly branched morphology of microglia under the PoRTS window that is indicative of nonactivation (three mice; **Supplementary Fig. 3**). We saw an essentially identical pattern on the control, contralateral hemisphere. We readily imaged submicrometer microglial processes, at depths greater than 100  $\mu\text{m}$  below the surface, over 2 months (**Supplementary Fig. 4**). Repeated imaging of the same general area showed a continued absence of activated microglia for all cases after installation of the PoRTS window (we

analyzed five mice at 2 d, three mice at 14 d, and three mice at 30 d; **Supplementary Fig. 5**).

A further assessment concerned reporters of brain trauma as evaluated in the area of cortex just below the PoRTS window. First, we assessed the expression of glial fibrillary acidic protein (GFAP), which is upregulated in reactive astrocytes during brain injury<sup>12</sup>. The pattern of immunostaining for GFAP was weak and indistinguishable from that seen in the control, contralateral hemisphere (three mice; **Supplementary Fig. 6**). This implies a lack of astrocyte activation. Second, we exploited the past finding that cortical injury can trigger remodeling and outgrowth of surface pial vasculature<sup>8</sup>. We observed that the pial surface vasculature remained nearly unchanged (two fields in each of two mice) with the PoRTS window (**Supplementary Fig. 7**). The astrocyte, microglia and vascular data collectively showed that the PoRTS window did not induce a classic inflammatory response in the brain. In contrast, we observed an increase in the density of brightly immunostained GFAP-positive astrocytes below a craniotomy (in all three mice analyzed), as well as an alteration of the vasculature topology (2 mice) that occurred primarily through the growth of surface veins after a craniotomy (**Supplementary Fig. 7**).

An application that exploits the large area of cortex that is visible through the PoRTS concerns the possibility of long-range correlations in vasomotion<sup>10</sup>, a 0.1–1 Hz oscillation in vascular tone that is hypothesized to be part of the ‘default’ state of brain activity<sup>13</sup>. We simultaneously measured the flow of red blood cells (RBCs) in pairs of subsurface microvessels, defined as vessels with diameters less than 7.5  $\mu\text{m}$ , in awake mice. We measured the RBCs in vessels over 100  $\mu\text{m}$  below the pial surface and separated by up to 500  $\mu\text{m}$  (17 mice measured up to 60 d after implantation of the window; **Fig. 2a–d**). As a population, the baseline speed was heterogeneous ( $0.90 \pm 0.61 \text{ mm s}^{-1}$ ; mean  $\pm$  s.d.; 159 vessels; **Supplementary Fig. 8**) and matched the values obtained for anesthetized rat<sup>10</sup>. Notably, low-frequency variations in blood flow were strongly and significantly

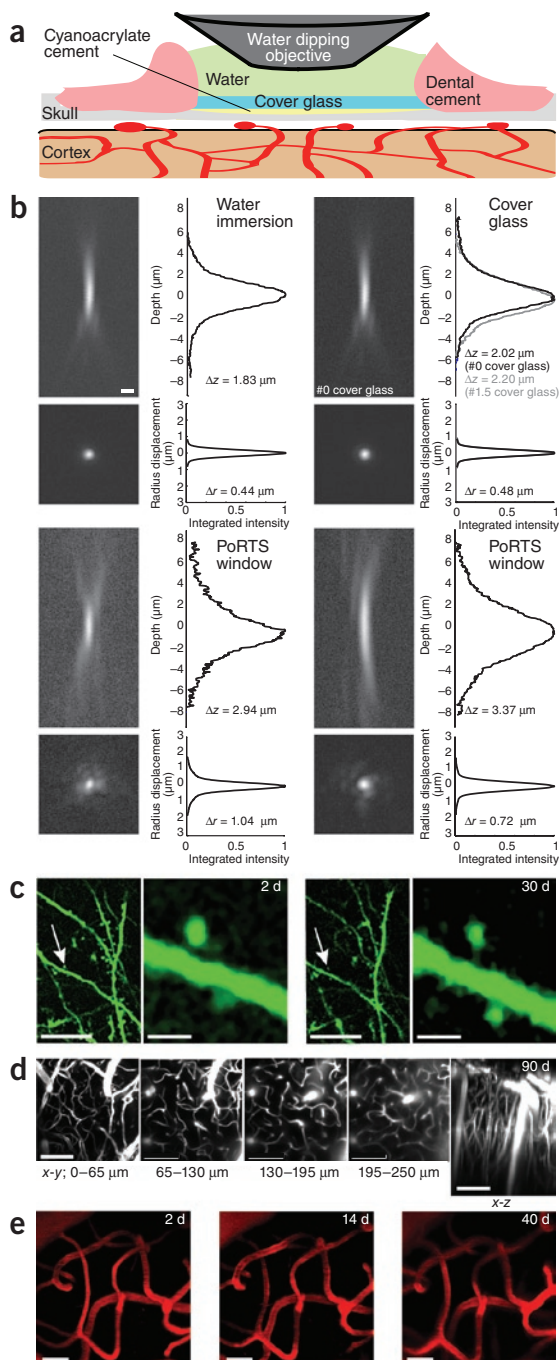


**Figure 1** | PoRTS window procedure, optical properties and basic capabilities. **(a)** Window schematic. The thinned and polished skull is protected with a cover glass attached with cyanoacrylate cement. Dental cement is used to seal the edge of the cover glass and provide support for the meniscus. The thinned area is typically 1–2 mm on edge. **(b)** Point spread functions for TPLSM determined by imaging 0.2- $\mu\text{m}$  fluorescent beads embedded in 1% (w/v) agarose with a 40 $\times$ , 0.8 numerical aperture (NA) water-dipping objective. The profiles show integrated radial intensity along the optical axis (z axis; depth), and integrated axial intensity along the radial axis (radius displacement). The reported axial resolution ( $\Delta z$ ) and radial width ( $\Delta r$ ) are the full widths that encompass half of the integrated intensity. The two sets of PoRTS data are for separate beads imaged through an excised PoRTS window. Scale bar, 1  $\mu\text{m}$ . **(c)** Representative fluorescence images of dendrites and spines of *thy1-YFP* neurons taken 30  $\mu\text{m}$  below the surface 2 d and 30 d (average of 5 frames owing to reduction in YFP signal) after PoRTS window implantation (dwell time, 6  $\mu\text{s pixel}^{-1}$ ; average incident power through the objective, 35–70 mW). Scale bars, 10  $\mu\text{m}$  (left image for each time point) and 1  $\mu\text{m}$  (close-up images of areas marked by arrows; right). **(d)** Maximum z-axis projections across 65  $\mu\text{m}$  of fluorescein-conjugated dextran-filled vasculature through a PoRTS window 90 d after surgery. Each image is the average of 6 frames; z-step, 2  $\mu\text{m}$ ; dwell time, 3  $\mu\text{s pixel}^{-1}$ ; and average power, 25–120 mW. Scale bars, 100  $\mu\text{m}$ . **(e)** Maximum projections across 20–70  $\mu\text{m}$  below the PoRTS window at indicated times after window implantation (average of 5 frames; dwell time, 6  $\mu\text{s pixel}^{-1}$ ; and average power, 30–45 mW). Scale bars, 100  $\mu\text{m}$ .

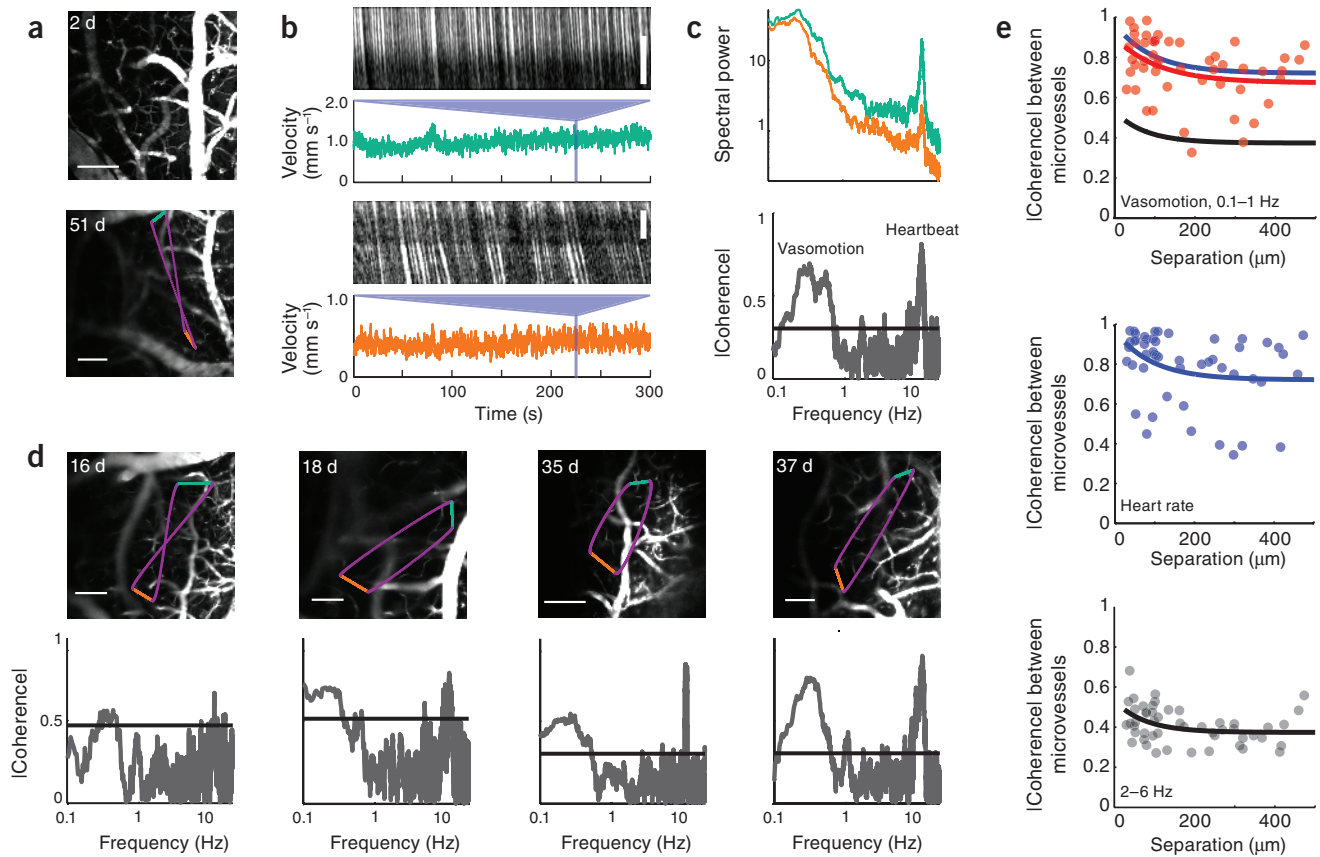


**Figure 2** | Long-range coherence of RBC-flow velocity in capillaries in the cortex of awake head-fixed mice through a PoRTS window. **(a)** Maximal z-dimension projection over 90  $\mu\text{m}$  of images of fluorescein-conjugated dextran-labeled vasculature, based on frames separated by 10  $\mu\text{m}$ , 2 d after surgery (top), and a single plane in the same mouse at a different location 51 d after surgery (bottom). Colored lines show the laser-focus scan path: green and orange are constant velocity segments along capillaries and purple are minimum time segments between capillaries. Scale bars, 100  $\mu\text{m}$ . **(b)** Space-time plots of one segment of line scan data for each of two capillaries, with the calculated instantaneous velocity for the entire 300 s run (bottom) for each constant-velocity segment shown in **a**. Scale bars, 10  $\mu\text{m}$ . **(c)** Power spectra for the two velocity traces in **b** (0.083 Hz bandwidth; top) and magnitude of the spectral coherence between the velocities of the two capillaries as a function of frequency (0.1 Hz bandwidth; bottom). **(d)** Spontaneous velocity coherence between capillaries obtained at various times after surgery; 0.1 Hz bandwidth. Representative data in **a–d** are from the same mouse obtained using a 10 $\times$ , 0.3 NA lens and averaged over 5–10 frames. Scale bars, 100  $\mu\text{m}$ . Lines in graphs in **c** and **d** denote  $P < 0.004$  (inverse of  $2 \times$  degrees of freedom). **(e)** Mean coherence as a function of distance in the 0.1–1.0 Hz vasomotor band (top), for the heart rate (positive control for the maximum possible coherence; middle) and in the 2–6 Hz band (null hypothesis; bottom). Fifty vessel pairs in nine mice were analyzed. Colored lines correspond to fits with exponential functions to the corresponding spectral band.

correlated out to 500  $\mu\text{m}$  ( $F_{2(n-2)}$  statistics, where  $n$  is the number of spectral estimators, typically 40; Fig. 2e), the longest separation we could probe. Coherence at the heart rate, which served as a positive control, was strongest between microvessels separated by less than 100  $\mu\text{m}$  and remained significant out to 500  $\mu\text{m}$ ; at intermediate frequencies we observed considerably less coherence. These data provide direct evidence for high spatial coherence of the 0.1–1.0 Hz vasomotion in awake mice.

Next we manipulated brain activity. A first application concerns the excitation of neurons expressing light-sensitive channels through the PoRTS window. We used a strain of mice that express channelrhodopsin-2 (ChR2) in the layer 5 pyramidal neurons, that is, *Thy1-YFP-ChR2*, and found that illumination of motor cortex with blue light elicited vibrissa movements (two awake mice analyzed; Fig. 3a,b). This shows that focal excitation of cells that express ChR2 is compatible with the PoRTS window. In a second application, we induced microstrokes via photosensitizers through

the PoRTS window. We induced an optically mediated occlusion to a single penetrating arteriole, the vessel that sources blood from the cortical surface to the parenchyma, by focal illumination of the intravenously injected photosensitizer Rose-Bengal with green laser light. This led to a localized clot (two mice analyzed; Fig. 3c,d). Occlusion of this single vessel was sufficient to produce a substantial infarct (Fig. 3e), as seen previously with a craniotomy<sup>14</sup>. Use of the PoRTS window allowed us to characterize the effects of experimental stroke on cortical viability while avoiding the possibility of additional damage from the craniotomy procedure. These examples show the utility of the PoRTS window for physiological manipulation in addition to imaging.

The PoRTS method enabled high-resolution chronic imaging and optical manipulation through large windows into the brain for at least 3 months. The windows did not require regular maintenance, did not induce an apparent inflammatory response, did not lead to vascular rearrangement, and may be used to image awake animals.

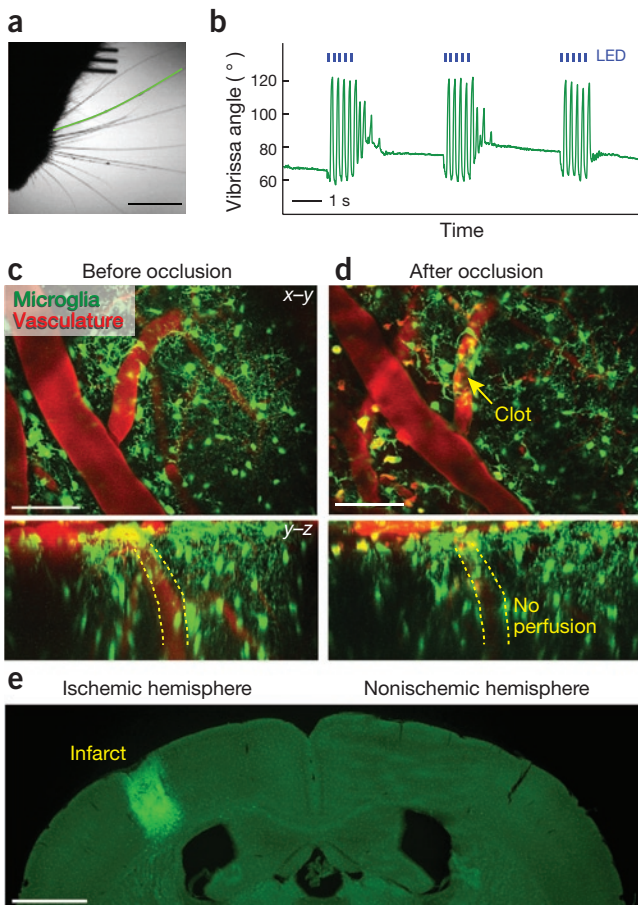


**Figure 3** | Examples of cortical physiology evoked through the PoRTS window. **(a)** Sample frame from video of an awake, head-fixed *ChR2*-carrying mouse with a PoRTS window fabricated over vibrissa motor cortex 150 d earlier. Green line marks the position of the caudal vibrissa that is tracked over time. **(b)** Rostral-caudal motion of a caudal vibrissa in response to 467-nm light pulses (5 Hz, 100-ms; blue lines) from an LED. Larger angles indicate retraction. **(c,d)** Maximal projection through a 200- $\mu$ m depth of a *Cx3cr1<sup>EGFP/+</sup>* mouse cortex before **(c)** and 100 min after **(d)** occlusion of a single penetrating arteriole using targeted optical activation of Rose Bengal (arrow) made 1 d after implantation of the window. Images are averages of four frames with a dwell time of 3  $\mu$ s per pixel and 1- $\mu$ m steps along the z axis. Dashed lines indicate the boundaries of the penetrating artery in which flow was blocked. **(e)** Extent of the infarct, for the same mouse as in **c** and **d**, visualized 2 d after the optically generated stroke. Note the invasion of EGFP-labeled microglia into the cyst. Scale bars, 5 mm **(a)**, 100  $\mu$ m **(c,d)** and 1 mm **(e)**.

US National Institutes of Health (EB003832, MH085499, NS059832 and RR021907 to D.K., and NS066361 to K.A.) and the Dana Program in Brain and Immunology (to K.A.) and fellowships from the Israeli Science Foundation (to P.B.), the Canadian Institutes of Health Research and American Heart Association (to A.Y.S.), the Human Frontiers Scientific Program (to P.M.K.), and the US National Multiple Sclerosis Society (to D.D.).

#### AUTHOR CONTRIBUTIONS

P.J.D., A.Y.S. and P.S.T. conceived the PoRTS window; J.D.D. and D.K. developed the imaging tools; K.A., D.D., P.J.D., D.K., A.Y.S. and P.S.T. designed the experiments; P.J.D., P.M.K., A.Y.S. and P.S.T. carried out the experiments; P.B., P.J.D., D.K. and P.S.T. analyzed data; and P.J.D., D.K. and A.Y.S. wrote the manuscript.

#### COMPETING FINANCIAL INTERESTS

The authors declare no competing financial interests.

Published online at <http://www.nature.com/naturemethods/>.

Reprints and permissions information is available online at <http://npg.nature.com/reprintsandpermissions/>.

- Svoboda, K., Denk, W., Kleinfeld, D. & Tank, D.W. *Nature* **385**, 161–165 (1997).
- Levasseur, J.E., Wei, E.P., Raper, A.J., Kontos, A.A. & Patterson, J.L. *Stroke* **6**, 308–317 (1975).
- Grutzendler, J., Kasthuri, N. & Gan, W.B. *Nature* **420**, 812–816 (2002).
- Trachtenberg, J.T. *et al. Nature* **420**, 788–794 (2002).
- Brown, C.E., Li, P., Boyd, J.D., Delaney, K.R. & Murphy, T.H. *J. Neurosci.* **27**, 4101–4109 (2007).
- Xu, H.T., Pan, F., Yang, G. & Gan, W.B. *Nat. Neurosci.* **10**, 549–551 (2007).
- Haus-Wegrzyniak, B., Lynch, M.A., Vraniak, P.D. & Wenk, G.L. *Exp. Neurol.* **176**, 336–341 (2002).
- Sohler, T.P., Lothrop, G.N. & Forbes, H.S. *J. Pharmacol. Exp. Ther.* **71**, 331–335 (1941).
- Holtmaat, A. *et al. Nat. Protoc.* **4**, 1128–1144 (2009).
- Kleinfeld, D., Mitra, P.P., Helmchen, F. & Denk, W. *Proc. Natl. Acad. Sci. USA* **95**, 15741–15746 (1998).
- Stoll, G. & Jander, S. *Prog. Neurobiol.* **58**, 233–247 (1999).
- Pekny, M. & Nilsson, M. *Glia* **50**, 427–434 (2005).
- Fox, M.D. & Raichle, M.E. *Nat. Rev. Neurosci.* **8**, 700–711 (2007).
- Blinder, P., Shih, A.Y., Rafie, C.A. & Kleinfeld, D. *Proc. Natl. Acad. Sci. USA* **107**, 12670–12675 (2010).
- Sawinski, J. *et al. Proc. Natl. Acad. Sci. USA* **106**, 19557–19562 (2009).

The downside of imaging through thinned bone was a loss in resolution, although this may be ameliorated through the use of adaptive optics to correct for distortions of the wavefront of the incident excitation beam. Lastly, the PoRTS window may be combined with miniaturized, head-mounted microscopes for chronic imaging in free-ranging animals<sup>15</sup>.

#### METHODS

Methods and any associated references are available in the online version of the paper at <http://www.nature.com/naturemethods/>.

Note: Supplementary information is available on the Nature Methods website.

#### ACKNOWLEDGMENTS

We thank B. Friedman, C. Portera-Cailliau and K. Svoboda for critical comments on an early version of the manuscript, M. Fuentes and C. Petersen for advice on head fixation, D.N. Hill for discussions on data analysis, J. Lee and K. Yang for help with animal husbandry, J.D. Moore for discussions on optical stimulation, and S. Tayman for a gift of tin oxide. This work was supported by grants from the

## ONLINE METHODS

**Surgery.** A detailed account of the surgical procedure leading to the PoRTS window is available in **Supplementary Note 1** and **Supplementary Figures 9** and **10**.

We used 37 mice for PoRTS windows and 11 for craniotomies. Adult C57/Bl6 mice were obtained from Charles River Laboratories, and transgenic mice were obtained from Jackson Labs. Adult heterozygous *Cx3cr1<sup>EGFP/+</sup>* mice<sup>16</sup> and heterozygous *Thy1-YFP H* line *ChR2* mice<sup>17</sup> were backcrossed with C57/Bl6 mice. Mice were males, 23 g or greater in mass, that were anesthetized with isoflurane, ~2% (v/v) in a 1:2 O<sub>2</sub> N<sub>2</sub>O mixture. In all mice in which craniotomies were performed, dexamethasone (Sigma; 0.08 mg per mouse) was administered. In a few cases, dexamethasone was also given to mice with PoRTS windows, but we observed no differences between animals with and without dexamethasone. As a prelude to both PoRTS window and craniotomy procedures, the scalp of mice was incised and resected. A head post was attached with a thin layer of cyanoacrylate cement followed by coverage in dental cement. In some mice, 2–3 small holes, ~0.25 mm in diameter, were drilled and self-tapping screws (3/32 inch diameter; Small Parts) were placed to help stabilize the skull. The mice were given antibiotics (Baytril, Bayer; 0.03 ml per mouse) and analgesics (Buprenex, Reckitt Benckiser Pharmaceuticals; 7 µg per mouse) at the conclusion of the surgery. Mice were habituated for 3–7 d to head fixation before imaging of blood flow in the awake mouse.

**PoRTS window.** An area up to 3 mm by 3 mm over the right somatosensory cortex was thinned using a high-speed handheld drill (K.1070 Micromotor Kit; Fore dome) based on published reports for rats<sup>18</sup> and mice<sup>3,19</sup>. Thinning was only performed for a few seconds at a time, and the skull was constantly wetted with an artificial cerebral spinal fluid (ACSF)<sup>20</sup> to prevent heating. During the thinning process, the drill bit was moved with the axis of rotation to minimize chatter and create a smoother surface for polishing. The final thickness of the skull was 10–15 µm, with the pial vessels clearly visible through the wetted bone. The skull was then sequentially polished with size 3F grit followed by size 4F grit (Convington Engineering) or polished with only tin oxide powder (Mama's Minerals). A slurry of grit and ACSF was agitated with a drill bit that had been dipped in silicone aquarium sealant (Perfecto Manufacturing) and withdrawn, leaving a tapered whip (**Supplementary Fig. 10**). Great care was taken not to apply pressure to the thinned portion of the skull. The first step in polishing was to apply a small amount of grit to the area to be polished and a drop of ACSF. The slurry was agitated by touching with the tip of the whip spinning at high speed, creating vortices in the slurry. The angle, position and rotational direction of the drill was varied such that the vortices polish the skull from all angles over a period of 5 to 10 min. After polishing, the skull was washed of grit and allowed to briefly dry. A drop of cyanoacrylate cement (31428 H04308; ND Industries) was put on the thinned region, and a pre-cut #0 cover glass was used to cap the cement. Excess cyanoacrylate cement was removed with a scalpel, and dental cement was used to seal the edges of the cover glass and form a berm around the window to help support a meniscus for imaging with dipping objectives. Widefield images of the vasculature were taken with a digital camera mounted on a dissection microscope (Stemi 500C; Zeiss).

'Failed' windows were usually caused by damage of pial blood vessels from excessive drill heat or pressure.

**Craniotomy.** An area of skull approximately 3 mm by 3 mm was thinned to ~50 µm as above, an incision around the margins was made with a 27.5-gauge needle, and the bone flap was gently removed<sup>9,20,21</sup>. The dura was left intact, and a cover glass was placed on the surface and sealed to the skull around the margins with dental cement. Great care was taken not to damage the dura and cortical surface, although one cannot discount the role of surgical skill in these preparations.

**Imaging and photostimulation.** *In vivo* two-photon imaging<sup>1</sup> was performed on a custom system<sup>22,23</sup> controlled by MPscope<sup>24,25</sup> with a Zeiss 10×, 0.3 NA dipping objective for the pial vessel montages (**Fig. 1c,d**) and Olympus 40×, 0.8 NA or 20×, 0.95 NA dipping objectives for all other datasets unless otherwise stated. The laser was tuned to 800 nm to image fluorescein and 870–920 nm to image EGFP and YFP or Texas red. The power at the laser focus was kept below 5 mW. Typically we were able to image the surface pial vessels with 10–25 mW average power, consistent with the measured attenuation of the TPLSM signal by a factor of  $e^{-1.5}$  through the thinned skull (**Supplementary Fig. 1**). Images were filtered with a 1-pixel median filter using Image J (<http://rsbweb.nih.gov/ij/>). For two-channel imaging, a 585-nm long-pass dichroic was used in combination with a blue-green glass filter (BG39; Andor Technology) on the green channel and an orange glass filter (OG590; Andor Technology) on the red channel. Mice were awake for functional imaging measurements (**Figs. 2a–d** and **3a,b**) and anesthetized with isoflurane, as described previously<sup>26,27</sup>, for structural imaging (**Figs. 1c–e** and **3c,d**).

**Blood flow.** Texas red conjugated to dextran (70 kDa; Invitrogen) or fluorescein conjugated to dextran (70 kDa; Sigma) were injected intravenously to visualize the vasculature<sup>10</sup>. Capillary RBC velocities were determined along single vessels or pairs of vessels with an arbitrary scan path<sup>28</sup> and use of the Radon transform method<sup>29</sup> to extract the speed of RBCs. In both craniotomies and thinned-skull preparations, dendritic cells<sup>30</sup> in the dura took up the injected Texas Red dextran over the hours after injection and remained labeled in subsequent imaging sessions.

**Neuronal photoexcitation.** Mice carrying a channelrhodopsin-2 gene under a *Thy1* promoter<sup>17</sup> backcrossed with C57/Bl6 had a PoRTS window fabricated over the right motor cortex (0.5 mm lateral of midline to 3 mm lateral and 1 mm posterior to Bregma to 2 mm anterior)<sup>31</sup>. An LED with 70 mW mm<sup>-2</sup> peak illumination power centered at 467 nm (ASMT-Mx00; Avago) was placed on top of the window and pulsed at 2 to 10 Hz to induce whisker motion. Vibrissa motions were captured at 500 Hz with a CMOS camera (A504k; Basler) and tracked offline using custom software<sup>32</sup>.

**Targeted photothrombosis.** Targeted clots in a single penetrating arteriole were initiated by illuminating the vessel with 532 nm laser light, focused to a 5 µm spot with the objective, immediately after injection of 50 µl of 1.25% (w/v) Rose Bengal in PBS through the infraorbital vein<sup>27,33</sup>.

**Histology.** Mice were perfused with 4% (w/v) paraformaldehyde in PBS (pH 7.4). The edge of the window was cut out around the cover glass with a high speed drill and the dye Evans blue was used to mark the boundaries of the window for later sectioning of the brain.

The brains were extracted and sunk in 30% (w/v) sucrose and 0.1% (w/v) sodium azide in PBS and sectioned at 50  $\mu\text{m}$ . Immunohistochemistry with antibody to GFAP was performed with a rabbit primary antibody (Invitrogen) at a 1:100 dilution and a goat anti-rabbit secondary antibody conjugated to the dye Alexa Fluor 594 (Invitrogen) diluted to 1:1,000. Histological images were taken with an Olympus MVX10 microscope or FV1000 confocal microscope.

**Point spread functions.** To evaluate image quality, we embedded subresolution, 0.2- $\mu\text{m}$  fluorescent beads in 1% (w/v) agarose and imaged them through an excised PoRTS window (Fig. 1b). An intensity distribution of the TPLSM signal from the bead,  $I(r, z)$ , was formed by stepping at an interval of 0.03  $\mu\text{m}$  along the  $z$  axis and sampling at 0.03  $\mu\text{m}$  along the  $x$  and  $y$  axes, with  $r = (x^2 + y^2)^{0.5}$ .

The reported widths,  $\Delta z$  and  $\Delta r$ , are the full height of an  $x$ - $y$  slab and the diameter of a cylinder along the  $z$  axis, respectively, that enclose half of the volume integrated intensity, that is, they are found through

$$2 \int_{-\Delta z}^{\Delta z} dz \int_0^{\infty} dr I(r, z) = \int_{-\infty}^{\infty} dz \int_0^{\infty} dr I(r, z)$$

and

$$2 \int_{-\infty}^{\infty} dz \int_0^{\Delta r} dr I(r, z) = \int_{-\infty}^{\infty} dz \int_0^{\infty} dr I(r, z)$$

These summary statistics account for intensity present in off-axis rings that are caused by aberrations. For comparison,  $\Delta z = 2.1 \mu\text{m}$  and  $\Delta r = 0.39 \mu\text{m}$  for imaging of a 0.02- $\mu\text{m}$  bead with an objective with NA = 0.8 and a uniformly illuminated back aperture<sup>34</sup>.

16. Jung, S. *et al. Mol. Cell. Biol.* **20**, 4106–4114 (2010).
17. Arenkiel, B.R. *et al. Neuron* **54**, 205–218 (2007).
18. Masino, S.A., Kwon, M.C., Dory, Y. & Frostig, R.D. *Proc. Natl. Acad. Sci. USA* **90**, 9998–10002 (1993).
19. Stosiek, C., Garaschuk, O., Holthoff, K. & Konnerth, A. *Proc. Natl. Acad. Sci. USA* **100**, 7319–7324 (2003).
20. Kleinfeld, D. & Delaney, K.R. *J. Comp. Neurol.* **375**, 89–108 (1996).
21. Denk, W. *et al. J. Neurosci. Methods* **54**, 151–162 (1994).
22. Tsai, P.S. & Kleinfeld, D. in *Methods for In Vivo Optical Imaging 2<sup>nd</sup> edn.* (ed., R.D. Frostig) 59–115 (CRC Press, 2009).
23. Tsai, P.S. *et al. Neuron* **39**, 27–41 (2003).
24. Nguyen, Q.-T., Dolnick, E.M., Driscoll, J. & Kleinfeld, D. in *Methods for In Vivo Optical Imaging 2<sup>nd</sup> edn.* (ed., R.D. Frostig) 117–142 (CRC Press, Boca Raton, 2009).
25. Nguyen, Q.-T., Tsai, P.S. & Kleinfeld, D. *J. Neurosci. Methods* **156**, 351–359 (2006).
26. Shih, A.Y. *et al. J. Cereb. Blood Flow Metab.* **29**, 738–751 (2009).
27. Shih, A.Y. *et al.* in *Imaging in Neuroscience and Development* (ed., R. Yuste) volume 2, chapter 15 (Cold Spring Harbor Laboratory Press, in the press).
28. Valmianski, I. *et al. J. Neurophysiol.* **104**, 1803–1811 (2010).
29. Drew, P.J., Blinder, P., Cauwenberghs, G., Shih, A.Y. & Kleinfeld, D. *J. Comput. Neurosci.* **29**, 5–11 (2010).
30. McMenamin, P.G. *J. Comp. Neurol.* **405**, 553–562 (1999).
31. Ferezou, I. *et al. Neuron* **56**, 907–923 (2007).
32. Knutsen, P.M., Derdikman, D. & Ahissar, E. *J. Neurophysiol.* **93**, 2294–2301 (2005).
33. Nishimura, N., Schaffer, C.B., Friedman, B., Lyden, P.D. & Kleinfeld, D. *Proc. Natl. Acad. Sci. USA* **104**, 365–370 (2007).
34. Born, M. & Wolf, E. *Principles of Optics: Electromagnetic Theory of Propagation Interference and Diffraction of Light 6th edn.* (Pergamon Press, Oxford, 1980).